Mon. Not. R. Astron. Soc. **392,** 346–360 (2009) doi:10.1111/j.1365-2966.2008.14058.x

Axisymmetric smoothed particle hydrodynamics with self-gravity

D. García-Senz,[1,2⋆] A. Relaño,[1⋆] R. M. Cabezón[1⋆] and E. Bravo[1,2⋆]
[1]*Departament de Física i Enginyeria Nuclear (UPC), Jordi Girona 3, Barcelona 08034, Spain*
[2]*Institut d'Estudis Espacials de Catalunya, Gran Capità 2-4, Barcelona 08034, Spain*

Accepted 2008 October 8. Received 2008 September 23; in original form 2008 June 27

ABSTRACT

The axisymmetric form of the hydrodynamic equations within the smoothed particle hydrodynamics (SPH) formalism is presented and checked using idealized scenarios taken from astrophysics (free fall collapse, implosion and further pulsation of a Sun-like star), gas dynamics (wall heating problem, collision of two streams of gas) and inertial confinement fusion (ablative implosion of a small capsule). New material concerning the standard SPH formalism is given. That includes the numerical handling of those mass points which move close to the singularity axis, more accurate expressions for the artificial viscosity and the heat conduction term and an easy way to incorporate self-gravity in the simulations. The algorithm developed to compute gravity does not rely in any sort of grid, leading to a numerical scheme totally compatible with the Lagrangian nature of the SPH equations.

Key words: methods: numerical.

1 INTRODUCTION

Since the smoothed particle hydrodynamics (SPH) method was proposed by Gingold & Monaghan (1977) and Lucy (1977) 30 yr ago, it has become a powerful and very successful method, which is routinely used worldwide to model systems with complicated geometries. In particular, the combination of the SPH method with hierarchical algorithms, addressed to efficiently organize data and calculate gravity, have led to a robust and reliable schemes able to handle complex geometries in three dimensions. In spite of these achievements, little effort has been put in the development of axisymmetric applications of the method. However, a large body of interesting applications has to do with systems which have axisymmetrical geometry such as accretion discs, rotating stars or explosive phenomena (i.e. novae or supernovae events) provided the ignition takes place in a point-like region at the symmetry axis. The interaction between the gas ejected during a supernova explosion and the circumstellar matter has been extensively simulated using cylindric coordinates either with Eulerian (Blondin, Lundqvist & Chevalier 1996) or SPH (Velarde et al. 2006) codes. In inertial confinement fusion (ICF) studies, the collapse of the deuterium capsule induced by laser ablation can be also approximated using two-dimensional hydrodynamics. Axisymmetrical hydrocodes are also useful to conduct resolution studies of three-dimensional codes just by imposing an initial configuration with the adequate symmetry. In these cases, a comparison between the results obtained using the three-dimensional hydrocode and the equivalent, although usually better resolved, two-dimensional simulation could help in numerical convergence studies. Several formulations of different complexity have been proposed to handle with the axisymmetric version of SPH. While the first algorithms were in general very crude [i.e. Herant & Benz (1992) and references therein] neglecting the so-called hoop-stress terms, there were also more consistent SPH approximations (Petscheck & Libersky 1993). Recently, more complete formulations were given by Brookshaw (2003) and Omang, Borve & Trulsen (2006). In particular, the scheme devised by Omang et al. includes not only the hoop-stress terms but also a consistent treatment of the singularity line defined by the symmetry axis. The algorithm proposed by these authors relies in the use of interpolative kernels especially adapted to the cylindrical geometry. Although the resulting scheme is robust, being able to successfully pass several test cases, it has the numerical inconvenient that an elliptical integral has to be solved numerically at each integration step for each particle.

In this paper, we propose a new formulation of the axisymmetric SPH technique which preserves many of the virtues stated by Brookshaw (2003) and Omang et al. (2006), being also able to handle the singularity axis in an efficient way. In our scheme, there is no necessity to modify the interpolating kernel (we use the cubic-spline polynomial). Instead, taking advantage of the symmetry properties across the Z-axis, we found several analytical correction factors to the physical magnitudes. These correction factors only affect particles moving at a distance from the Z-axis lesser than $2h$, being h the smoothing-length parameter. For the remaining particles, the SPH equations are identical to those given in Brookshaw (2003). In addition, we also give expressions for the artificial viscosity and a new heat conduction algorithm, which takes into account the hoop-stress contribution. Finally, we propose an original method to handle gravity within the SPH paradigm which is consistent with the gridless nature of that particle method. The text is organized as follows. The

⋆E-mail: domingo.garcia@upc.edu (DG-S); antonio.relano@upc.edu (AR); ruben.cabezon@upc.edu (RMC); eduardo.bravo@upc.edu (EB)

basic fluid equations written in axisymmetric coordinates, and corrected from axis effects when necessary, are provided in Section 2. In Section 3, we add useful physics to these equations consisting of an artificial viscosity term to handle shock waves (Section 3.1), an expression for thermal conduction (Section 3.2) and an algorithm addressed to calculate self-gravity within the axisymmetric hypothesis (Section 3.3). Section 4 is devoted to describe and discuss five test cases aimed at validating the proposed scheme. Finally, the main conclusions of our work as well as some comments about the limitations of the developed scheme and prospects for the future are presented in Section 5.

2 FLUID EQUATIONS IN THE AXISYMMETRIC APPROACH

An elegant approach to the axisymmetric Euler fluid equations was given by Brookshaw (2003) who derived the SPH form of these basic equations using the minimal action principle (see Monaghan 2005, and references therein for the history of variational SPH). The resulting expressions for mass, momentum and energy conservation written in the cylindrical coordinate system $\boldsymbol{s} = (r, z)$ are

$$\eta_i = \sum_{j=1}^{N} m_j W_{ij}, \tag{1}$$

$$\begin{cases} \ddot{r} = 2\pi \frac{P_i}{\eta_i} - 2\pi \sum_{j=1}^{N} m_j \left(\frac{P_i r_i}{\eta_i^2} + \frac{P_j r_j}{\eta_j^2} \right) \frac{\partial W_{ij}}{\partial r_i} \\ \ddot{z} = -2\pi \sum_{j=1}^{N} m_j \left(\frac{P_i r_i}{\eta_i^2} + \frac{P_j r_j}{\eta_j^2} \right) \frac{\partial W_{ij}}{\partial z_i}, \end{cases} \tag{2}$$

$$\frac{\mathrm{d}u_i}{\mathrm{d}t} = -2\pi \frac{P_i v_{r_i}}{\eta_i} + 2\pi \frac{P_i r_i}{\eta_i^2} \sum_{j=1}^{N} m_j (\boldsymbol{v_i} - \boldsymbol{v_j}) \cdot \boldsymbol{D}_i W_{ij}, \tag{3}$$

where $\eta_i = 2\pi\, r_i \rho_i$ is the two-dimensional density of the i-particle, $\boldsymbol{v} = (v_r, v_z)$ its velocity, $W_{ij} = W_{ij}\left(\frac{|s_i - s_j|}{h_i}\right)$ the interpolating kernel and the remaining symbols have their usual meaning. The differential operator $\boldsymbol{D} = (\frac{\partial}{\partial r}, \frac{\partial}{\partial z})$ is a Cartesian operator written in the (r, z) plane of cylindric coordinates. The first terms on the right in the r-component of equations (2) and (3) are called the hoop-stress terms. They are geometrical terms which arise from the nabla operator written in cylindrical coordinates. The smoothing-length parameter, h, is usually taken as the local resolution of the SPH. Equations (1)–(3) along with the adequate equation of state (EOS) are the starting point to carry out numerical simulations of fluid systems with axisymmetric geometry. As boundary conditions we consider reflective ghost particles across the Z-axis and open flow at the outer limits of the system. For the i-particle with coordinates (r_i, z_i) and velocity $(\dot{r}_i, \dot{z}_i)$, it is defined its reflective k-particle by taking $(r_k, z_k) = (-r_i, z_i)$, $(\dot{r}_k, \dot{z}_k) = (-\dot{r}_i, \dot{z}_i)$ and $m_k = m_i$. Thus, position, velocity as well as other magnitudes such as density or internal energy of reflective particles are updated at each step not using the SPH equations but from the evolution of real particles. Even though the use of reflective boundary conditions is not strictly necessary in axisymmetric geometry, it is useful to correctly represent the density and its derivatives near to the singularity axis.

2.1 Correction terms close to the singularity axis

One of the major causes of inaccuracy of axisymmetric SPH is the treatment of particles that get close to the symmetry axis. Unlike spherically symmetric systems, there is only one singular point, just at the centre, here is a singular line at $r = 0$. A good treatment of particles moving close to the Z-axis is especially relevant for implosions such as the collapse of a self-gravitating system or in ICF studies. As far as we know only Omang et al. (2006) have consistently addressed this problem. In that paper, the interpolation kernel is modified according to the particular geometry of the system, spherical or cylindrical. The resulting scheme does not have singularity problems when the particles approach the axis. However, the resulting kernel does not have an analytical expression and must be calculated at any step for each particle using a numerical integration. Recently, useful fitting formulae were proposed by Omang, Borve & Trulsen (2007) but still involving a large number of operations which slows the calculation.

An alternative way to handle with the symmetry axis, without modifying the basic SPH scheme given above, is to calculate correction terms to equations (1)–(3), which become significant only close to the Z-axis. These correction factors arise because of the limited capability of standard kernels to interpolate accurately non-linear functions. In the particular case of the two-dimensional density, $\eta = 2\pi |\, r|\rho$, its profile is not longer linear in the axis neighbourhoods due to the presence of reflective particles. Usually, the errors are small and the interpolation is precise to second order in h. Unfortunately, close to the symmetry axis errors grow and density and other physical magnitudes are not well reproduced, as it will be shown below. The detailed derivation of these corrections are given in Appendix A, leading to the following equations:

$$\widehat{\eta}_i = \sum_{j=1}^{N} m_j W_{ij} \times f_1^i = \eta_i \times f_1^i, \tag{4}$$

where $\widehat{\eta}_i$ is the new, improved, two-dimensional density and f^i_1 is a correction factor which, for the cubic-spline kernel, reads (Appendix A)

$$f_1^i = \begin{cases} \left[\frac{7}{15}\zeta_i^{-1} + \frac{2}{3}\zeta_i - \frac{1}{6}\zeta_i^3 + \frac{1}{20}\zeta_i^4 \right]^{-1} & 0 < \zeta_i < 1 \\ \left[\frac{8}{15}\zeta_i^{-1} - \frac{1}{3} + \frac{4}{3}\zeta_i - \frac{2}{3}\zeta_i^2 + \frac{1}{6}\zeta_i^3 - \frac{1}{60}\zeta_i^4 \right]^{-1} & \text{for} \quad 1 < \zeta_i < 2 \\ 1 & \zeta_i > 2 \end{cases} \tag{5}$$

being $\zeta_i = r_i/h_i$. A plot of $f_1(\zeta)$ and its first derivative is given in Fig. 1. Hereafter, a hat will be placed over any corrected, and therefore, 'true' magnitude.

At this point, it is useful to introduce a couple of algebraic rules:

$$\widehat{A}_i = \sum_j m_j \frac{A_j}{\widehat{\eta}_j} W_{ij} \tag{6}$$

$$\widehat{\eta A}_i = f_1^i \sum_j m_j A_j W_{ij}, \tag{7}$$

which are valid as long as, close to the axis, the magnitude A has a weak dependence in the r-coordinate. In particular, setting $A = 1$ in equation (7) leads to equation (4).

To find the influence of the above correction factor in the momentum equation, equation (2), it is better to write the components of that equation in differential form. For the radial component, we have:

$$\ddot{r} = -\frac{1}{\rho}\frac{\partial P}{\partial r} = -\frac{2\pi r}{\widehat{\eta}}\frac{\partial P}{\partial r} = 2\pi \frac{P}{\widehat{\eta}} - \frac{2\pi r P}{\widehat{\eta}^2}\frac{\partial \widehat{\eta}}{\partial r} - \frac{\partial}{\partial r}\left(\frac{2\pi r P}{\widehat{\eta}}\right). \tag{8}$$

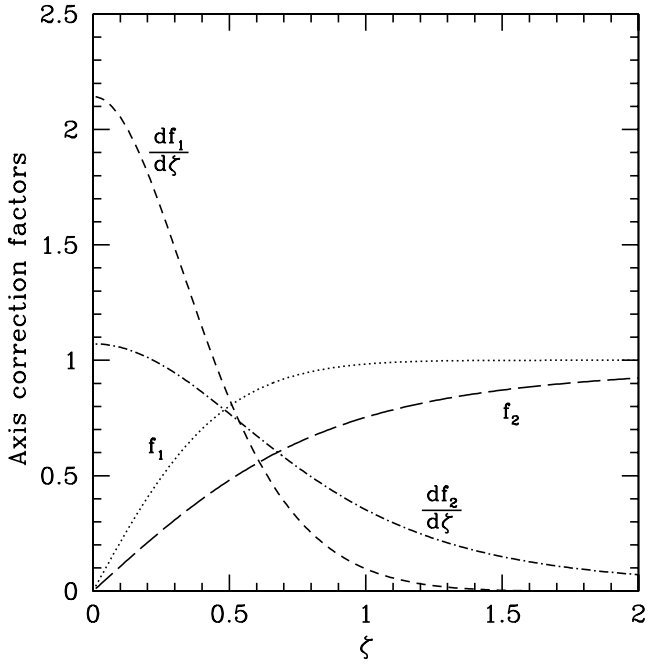

Figure 1. Plot of the correction factors f_1 and f_2 and their derivatives as a function of $\zeta = r/h$. The cubic spline interpolator kernel was assumed to compute f_1 and f_2 (Appendix A).

When $r \to 0$ the particle approaches the Z-axis where symmetry enforces the last term on the right to vanish for spherically symmetric kernels. The first term on the right is the hoop-stress term which should be exactly balanced by the central term when $r \to 0$, because the acceleration should be zero at the symmetry axis. Nevertheless, this does not happen unless the correction factor $f_1(\zeta)$ is taken into account during the calculation of the gradient of $\widehat{\eta}$,

$$\frac{\partial \widehat{\eta}}{\partial r} = \frac{\partial [f_1(\zeta)\eta]}{\partial r} = f_1(\zeta)\frac{\mathrm{d}\eta}{\mathrm{d}r} + \eta\frac{\partial f_1(\zeta)}{\partial r}. \tag{9}$$

Similarly, for the Z-component in the momentum equation:

$$\ddot{z} = -\frac{1}{\rho}\frac{\partial P}{\partial z} = -\frac{2\pi r}{\widehat{\eta}}\frac{\partial P}{\partial z} = -\frac{2\pi r P}{\widehat{\eta}^2}\frac{\partial \widehat{\eta}}{\partial z} - \frac{\partial}{\partial z}\left(\frac{2\pi r P}{\widehat{\eta}}\right), \tag{10}$$

where now we simply have:

$$\frac{\partial \widehat{\eta}}{\partial z} = f_1(\zeta)\frac{\partial \eta}{\partial z}. \tag{11}$$

The resulting momentum components in discrete SPH form can be obtained from equations (6) to (11):

$$\ddot{r}_i = 2\pi\frac{P_i}{\widehat{\eta}_i} - 2\pi\sum_{j=1}^{N}\left\{m_j\left[\frac{P_i r_i}{\widehat{\eta}_i^2}\times f_1^i(\zeta_i) + \frac{P_j r_j}{\widehat{\eta}_j^2}\right]\frac{\partial W_{ij}}{\partial r_i}\right\} - \left(\frac{2\pi P_i r_i}{\widehat{\eta}_i \times f_1^i}\right)\frac{\mathrm{d}f_1^i(\zeta_i)}{\mathrm{d}r_i}, \tag{12}$$

$$\ddot{z}_i = -2\pi\sum_{j=1}^{N} m_j\left[\frac{P_i r_i}{\widehat{\eta}_i{}^2}\times f_1^i(\zeta_i) + \frac{P_j r_j}{\widehat{\eta}_j{}^2}\right]\frac{\partial W_{ij}}{\partial z_i}. \tag{13}$$

The value of pressure in equations (12) and (13) must be computed through the EOS using the 'corrected' three-dimensional density, $\widehat{\rho} = \widehat{\eta}/(2\pi r)$.

Note that close to the axis the summatories in equations (12) and (13) are non-symmetric with respect any pair of particles. Still the r-component of the momentum is conserved, even for those particles with $r < 2h$, because of the imposed reflective boundary conditions. In the Z-axis, the momentum is not exactly conserved within the band defined by $r < 2h$. In general, such loss is small, affecting a tiny amount of mass. In most of the tests described below, total momentum was very well preserved.

A similar approach can be worked out to improve the energy equation:

$$\frac{\mathrm{d}u}{\mathrm{d}t} = -2\pi\frac{P}{\widehat{\eta}}v_r + 2\pi\frac{Pr}{\widehat{\eta}^2}\frac{\mathrm{d}\widehat{\eta}}{\mathrm{d}t}, \tag{14}$$

where

$$\frac{\mathrm{d}\widehat{\eta}}{\mathrm{d}t} = \left[v_r\frac{\partial \widehat{\eta}}{\partial r} - \frac{\partial(\widehat{\eta v_r})}{\partial r}\right] + \left[v_z\frac{\partial \widehat{\eta}}{\partial z} - \frac{\partial(\widehat{\eta v_z})}{\partial z}\right] \tag{15}$$

being $\widehat{\eta} = \eta \times f_1$; $\widehat{(\eta v_z)} = (\eta v_z) \times f_1$ and $\widehat{(\eta v_r)} = (\eta v_r) \times f_2$. The factor f_2 is (Appendix A)

$$f_2^i = \begin{cases} \left[\frac{14}{15}\zeta_i^{-1} + \frac{4}{9}\zeta_i - \frac{1}{15}\zeta_i^3 + \frac{1}{60}\zeta_i^4\right]^{-1} & 0 < \zeta_i < 1 \\ \left[-\frac{1}{45}\zeta_i^{-2} + \frac{16}{15}\zeta_i^{-1} - \frac{1}{3} + \frac{8}{9}\zeta_i - \frac{1}{3}\zeta_i^2 + \frac{1}{15}\zeta_i^3 - \frac{1}{180}\zeta_i^4\right]^{-1} & \text{for} \quad 1 < \zeta_i < 2 \\ 1 & \zeta_i > 2. \end{cases} \tag{16}$$

The resulting energy equation in discrete SPH form is

$$\frac{\mathrm{d}u_i}{\mathrm{d}t} = -2\pi\frac{P_i}{\widehat{\eta}_i}v_{r_i} + 2\pi\frac{P_i r_i}{\widehat{\eta}_i{}^2}\frac{\mathrm{d}\widehat{\eta}_i}{\mathrm{d}t}, \tag{17}$$

where

$$\frac{\mathrm{d}\widehat{\eta}_i}{\mathrm{d}t} = \sum_{j=1}^{N} m_j\left(f_1^i v_{r_i} - f_2^i v_{r_j}\right)\frac{\partial W_{ij}}{\partial r_i} + \sum_{j=1}^{N} m_j\left(\frac{\partial f_1^i}{\partial r_i}v_{r_i} - \frac{\partial f_2^i}{\partial r_i}v_{r_j}\right)W_{ij} + f_1^i\sum_{j=1}^{N} m_j\left(v_{z_i} - v_{z_j}\right)\frac{\partial W_{ij}}{\partial z_i}. \tag{18}$$

Note that f_1^i, f_2^i and their derivatives are only function of the current radial coordinate of the particle and its smoothing length. Thus, they can easily be computed and stored in a vector without introducing any significant computational overload. Examples about the use of the axisymmetric fluid equations with axis corrections, equations (4), (12), (13) and (17) in practical situations will be provided and discussed in Section 4.

3 ADDING PHYSICS: SHOCKS, THERMAL CONDUCTION AND GRAVITY

3.1 Artificial viscosity

As in three dimensions, the treatment of shocks in the axisymmetric approach also relies in the artificial viscosity formalism. None the less, there are a variety of artificial viscosity algorithms suited for SPH to choose at. We have adapted the standard recipe by Monaghan & Gingold (1983) to the peculiarities of the two-dimensional axisymmetric hydrodynamics. In that approach, the artificial viscosity gives rise to a viscous bulk and shear pressure which is added to the normal gas pressure only in those regions

where the particles collide (in the SPH sense[1]). In three dimensions, it is defined a magnitude, Π_{ij}:

$$\Pi_{ij}^{3D} = \begin{cases} \frac{-\alpha_0 \bar{c}_{ij}\mu_{ij}+\beta_0\mu_{ij}^2}{\bar{\rho}_{ij}} & \boldsymbol{v_{ij}}\cdot\boldsymbol{r_{ij}} < 0 \\ 0 & \boldsymbol{v_{ij}}\cdot\boldsymbol{r_{ij}} > 0, \end{cases} \tag{19}$$

which is closely related to the viscous pressure. In equation (19), α_0 and β_0 are constants of the order of unity, $\bar{\rho}_{ij}$ and $\bar{c}_{ij}$ are the average of density and sound speed of i and j- particles, and μ_{ij} is

$$\mu_{ij} = \frac{h_{ij}\boldsymbol{v}_{ij}\cdot\boldsymbol{r}_{ij}}{r_{ij}^2+\nu^2}, \tag{20}$$

here $\boldsymbol{v}_{ij} = (\boldsymbol{v}_i - \boldsymbol{v}_j)$, $\boldsymbol{r}_{ij} = (\boldsymbol{r}_i - \boldsymbol{r}_j)$ and $\nu = 0.1h$ avoid divergences when $r_{ij} \to 0$. The scalar magnitude Π_{ij} has a linear and a quadratic term. The linear component mimics bulk and shear viscosity of fluids whereas the quadratic one is important to avoid particle interpenetration in strong shocks.

The easiest way to write the contribution of the artificial viscosity to the momentum and energy equations in an axisymmetric code is by changing the mass of the particles according to their distance to the Z-axis: $m \longrightarrow m/2\pi r$. The viscous acceleration becomes

$$\boldsymbol{a}_i^{\rm vis} = \sum_{j=1}^{N} \frac{m_j}{2\pi\bar{r}_{ij}}\Pi_{ij}^{3D}\boldsymbol{D}_i W_{ij}. \tag{21}$$

Taking $\bar{\rho}_{ij} = \bar{\eta}_{ij}/(2\pi\bar{r}_{ij})$, in equation (19), the explicit dependence on r_{ij} in the viscous acceleration formula is removed,

$$\boldsymbol{a}_i^{\rm vis} = \sum_{j=1}^{N} m_j \Pi_{ij}^{(1)}\boldsymbol{D}_i W_{ij}, \tag{22}$$

where $\Pi_{ij}^{(1)}$ is

$$\Pi_{ij}^{(1)} = \begin{cases} \frac{-\alpha_0\bar{c}_{ij}\mu_{ij}+\beta_0\mu_{ij}^2}{\bar{\bar{\eta}}_{ij}} & \boldsymbol{v_{ij}}\cdot\boldsymbol{s_{ij}} < 0 \\ 0 & \boldsymbol{v_{ij}}\cdot\boldsymbol{s_{ij}} > 0 \end{cases}, \tag{23}$$

being μ_{ij}:

$$\mu_{ij} = \frac{h_{ij}\boldsymbol{v}_{ij}\cdot\boldsymbol{s}_{ij}}{s_{ij}^2+\nu^2}. \tag{24}$$

Expressions (22)–(24) account for the Cartesian part of viscosity. It has been shown (i.e. Monaghan 2005) that, in the continuous limit, these expressions become the Navier–Stokes equations provided shear and bulk viscosity coefficients are taken $\eta_{\rm vis} = \rho\alpha_0 hc/8$ and $\zeta_{\rm vis} = 5\eta_{\rm vis}/3$, respectively. However, in cylindric geometry, the stress tensor which appears in the Navier–Stokes equations also includes a term proportional to velocity divergence through the so-called second viscosity coefficient. Therefore, an extra term containing the magnitude (v_r/r) must be added to $\Pi_{ij}^{(1)}$ to account for the convergence of the flux towards the axis. This new term, $\Pi_{ij}^{(2)}$, should fulfil a few basic requirements. (1) Far enough from the axis it should be negligible, (2) must vanish for those particles with $v_r \geq 0$, (3) for homologous contractions the viscous acceleration related to that term should be negligible, (4) it should be symmetric with respect particles i and j to conserve momentum. An expression satisfying the four items is

$$\Pi_{ij}^{(2)} = \begin{cases} \frac{-\alpha_1\bar{c}_{ij}q_{ij}+\beta_1 q_{ij}^2}{\bar{\bar{\eta}}_{ij}} & v_{r_i} \text{ and } v_{r_j} < 0 \\ 0 & \text{othercases} \end{cases} \tag{25}$$

[1] In the SPH method, the so-called particles could be looked as finite spheres of radii $2h$.

where $q_{ij} = 0.5(\frac{h_i v_{r_i}}{r_i} + \frac{h_j v_{r_j}}{r_j})$. The resulting viscous acceleration is

$$\boldsymbol{a}_i^{vis} = \sum_{j=1}^{N} m_j \Pi_{ij}^{2D}\boldsymbol{D}_i W_{ij}, \tag{26}$$

where $\Pi_{ij}^{2D} = \Pi_{ij}^{(1)} + \Pi_{ij}^{(2)}$. Note that for a homologous contraction $v_r \propto r$ meaning $q \simeq$ const., hence the gradient of $< \eta\Pi^{(2)} >$ vanishes fulfilling the third requirement above. In diverging shocks, $\Pi_{ij}^{(2)}$ vanishes and only the Cartesian part of viscosity matters. Therefore, constants α_0, β_0 should remain close to their standard values $\alpha_0 \simeq 1$ and $\beta_0 \simeq 2$. All simulations presented in this paper were carried out using $\alpha_1 = \alpha_0 = 1$, $\beta_1 = \beta_0 = 2$. In converging shocks, however, the effect of $\Pi_{ij}^{(2)}$ is to increase artificial viscosity introducing more damping in the system.

Equation (26) has the advantage that is formally similar to that used in three dimensions. Therefore, one can benefit from the well-known features of the artificial viscosity in three dimensions, which can be directly translated to the axisymmetric version (several useful variations of equation 19 can be found in Monaghan 2005). In particular, it is straightforward to write the corresponding energy equation:

$$\left(\frac{{\rm d}u_i}{{\rm d}t}\right)_{\rm vis} = \frac{1}{2}\sum_{j=1}^{N} m_j \Pi_{ij}^{2D}(\boldsymbol{v_i} - \boldsymbol{v_j})\cdot\boldsymbol{D}_i W_{ij}, \tag{27}$$

which has to be added to the right-hand side of equation (3).

3.2 An approach to the conduction term

The differential equation describing the evolution of the specific internal energy due to conductive or diffusive heat transfer is

$$\left(\frac{{\rm d}u}{{\rm d}t}\right)_{\rm cond} = \frac{1}{\rho}\boldsymbol{\nabla}\cdot(\kappa\boldsymbol{\nabla}T) \tag{28}$$

being κ the conductivity coefficient which in turn is a function of the local thermodynamic state of the material. The main difficulty to write equation (28) in a discrete equation suitable to SPH calculations is the existence of a second derivative. It is well known that second and higher order derivatives often pour a lot of numerical noise in disordered systems. A way to avoid that shortcoming is to reduce one degree the order of the derivative by taking the integral expression of equation (28), Brookshaw (1985). It has been shown (see, for example, Jubelgas, Springel & Dolag 2004) that in three-dimensional Cartesian coordinates the following expression allows to approximate a second derivative using only the first derivative of the interpolation kernel:

$$(\nabla^2 Y)_i = 2\sum_{j=1}^{N}\frac{m_j}{\rho_j}\frac{Y_j - Y_i}{r_{ij}^2}\boldsymbol{r}_{ij}\cdot\boldsymbol{\nabla_i W_{ij}}, \tag{29}$$

where Y represents any scalar magnitude and $\boldsymbol{r}_{ij} = \boldsymbol{r}_i - \boldsymbol{r}_j$. An useful algebraic relationship which allows to write the heat transfer equation in SPH notation is

$$\boldsymbol{\nabla}\cdot(\kappa\boldsymbol{\nabla T}) = \frac{1}{2}[\nabla^2(\kappa T) - T\nabla^2\kappa + \kappa\nabla^2 T]. \tag{30}$$

Combining equations (29) and (30), the usual form of the heat transfer equation used in three-dimensional SPH studies is obtained. A mathematical expression for the heat transfer equation in axisymmetric SPH was given by Brookshaw (2003). However, in the derivation of equation (29), there was not taken into account the $\simeq 1/r$ term which naturally arises whenever the divergence of a

vector is estimated in cylindric coordinates:

$$\nabla \cdot (\nabla Y) = \frac{1}{r}\left(\frac{\partial Y}{\partial r}\right) + \frac{\partial}{\partial r}\left(\frac{\partial Y}{\partial r}\right) + \frac{\partial}{\partial z}\left(\frac{\partial Y}{\partial z}\right). \quad (31)$$

It will be shown in Section 4.1 how the inclusion of the first term on the right of equation (31) improves the quality of the results in a particular test.

To obtain the adequate numerical approximation to equation (28) in axisymmetric SPH, we first make use of equation (30):

$$\left(\frac{\mathrm{d}u}{\mathrm{d}t}\right)_{\mathrm{cond}} = \frac{1}{2\rho}\{\nabla^2(\kappa T) - T\nabla^2\kappa + \kappa\nabla^2 T\}. \quad (32)$$

Then, using equation (31) to develop each term inside the brackets and using the two-dimensional operator $\boldsymbol{D} \equiv (\frac{\partial}{\partial r}, \frac{\partial}{\partial z})$ instead of ∇ the following expression is obtained:

$$\left(\frac{\mathrm{d}u_i}{\mathrm{d}t}\right)_{\mathrm{cond}} = \frac{1}{2\rho}\left\{\frac{1}{r_i}\frac{\partial(\kappa T_i)}{\partial r_i} - \frac{T_i}{r_i}\frac{\partial \kappa_i}{\partial r_i} + \frac{\kappa_i}{r_i}\frac{\partial T_i}{\partial r_i}\right\} + \frac{1}{\rho_i}\sum_{j=1}^{N}\left[m_j\frac{\kappa_i+\kappa_j}{\widehat{\eta}_j}(T_i - T_j)\frac{\boldsymbol{s}_{ij}}{s_{ij}^2}\cdot \boldsymbol{D}_i W_{ij}\right]. \quad (33)$$

The magnitudes inside the brackets are the new terms related to the hoop stress. In order to calculate the derivatives, we make use of one of the golden rules of SPH (Monaghan 2005):

$$\frac{\partial C_i}{\partial r_i} = \sum_j \frac{m_j}{\widehat{\eta}_j}(C_j - C_i)\frac{\partial W_{ij}}{\partial r_i}. \quad (34)$$

After a little algebra, the following expression is obtained:

$$\left(\frac{\mathrm{d}u_i}{\mathrm{d}t}\right)_{\mathrm{cond}} = -\pi\sum_{j=1}^{N} m_j\frac{(\kappa_i+\kappa_j)}{\widehat{\eta}_i\widehat{\eta}_j}(T_i - T_j)\frac{\partial W_{ij}}{\partial r_i} + 2\pi r_i\sum_{j=1}^{N} m_j\frac{(\kappa_i+\kappa_j)}{\widehat{\eta}_i\widehat{\eta}_j}(T_i - T_j)\frac{\boldsymbol{s}_{ij}}{s_{ij}^2}\cdot \boldsymbol{D}_i W_{ij}. \quad (35)$$

The presence of $(T_i - T_j)$ in the equation ensures that there is not heat flux between different parts of an isothermal system. Note that the presence of the r_i multiplier in the second term in the right-hand side of equation (35) does not ensure complete conservation of the heat flux. However, the total energy losses in the numerical test below simulating a thermal wave evolution were negligible. Of course equation (35) can be symmetrized by taking the arithmetical mean $\bar{r}_{ij}$ instead of r_i but in that case the evolution of the thermal wave was not so well reproduced. On another note, equation (35) is compatible to the second principle of thermodynamics in the sense that heat always flows from high to low temperature particles. To demonstrate this, let us take a pair of particles i and j so that $T_i > T_j$. The second term on the right-hand side becomes negative because the scalar product $\boldsymbol{s}_{ij}\cdot DW_{ij}/ds_i$ is always negative. The first term on the right-hand side is negative for $r_i < r_j$ and positive for $r_i > r_j$. As the heat flow from particle i must be negative the only trouble could come if $r_i > r_j$. Nevertheless, even in that case heat flux is still negative if $r_i/(r_i - r_j) > 1/2$ because the sign of the second term in equation (35) prevails. Thus, $r_i/(r_i - r_j) > 1/2$ is a sufficient condition to get the right sign of heat flux between any pair of particles. As $r_i - r_j \simeq h$ such condition is fulfilled in a large domain of the system. The exception could be the axis vicinity, where $r_i \to 0$. Nevertheless, in that case symmetry enforces the heat flux to be negligible. Therefore, we expect a good behaviour of the heat flux arrow although there are not excluded marginal violations if resolution is poor and strong heat fluxes were present close to $r = 0$. A way to ensure complete compatibility to the second principle of thermodynamics is to make zero the flux between any pair of particles violating such principle.

3.3 Self-gravity

Current two-dimensional hydrocodes often handle gravity by solving the Poisson equation or, if the system remains nearly spherical, by simply computing the enclosed Lagrangian mass in a sphere below the point and using the Gauss law. Methods based on the Poisson solvers have proven very useful to find gravity in Eulerian hydrodynamics where the same grid used to compute the motion of the fluid elements can be used in the calculation of gravity. However, they have the difficulty to set suitable outer boundary conditions owing to the infinite range of the gravitational force. In Lagrangian gridless methods such as SPH, it is better to use the direct interaction among mass particles themselves to calculate gravity. The evaluation of the gravitational force through direct particle–particle interaction leads to an N^2 scheme that makes the computation feasible only for a limited number of particles. When N is high, as it is frequent in three-dimensional calculations, one has to rely in approximate schemes such as those based in hierarchical-tree methods, Hernquist & Katz (1989). However, hierarchical methods do not work efficiently in the two-dimensional axisymmetric approach because what we call particles are in fact rings of different size. Usually, the ratio between the radius of these rings and the distance to the point where the force needs to be computed is too large to permit the multipolar approach to evaluate the gravitational force. Fortunately, the good resolution usually achieved in two dimensional codes using a moderate number of particles makes the direct calculation affordable.

According to Fig. 2, the gravitational force per unit of mass in a point P of coordinates $(0, y_{\mathrm{p}}, z_{\mathrm{p}})$ (being Z the symmetry axis) due to the ring is

$$\boldsymbol{g}(0, y_{\mathrm{p}}, z_{\mathrm{p}}) = G\int_0^{2\pi}\frac{\rho R\mathrm{d}\varphi}{(R^2 + s'^2 - 2y_{\mathrm{p}}R\sin\varphi)^{3/2}} \times[(R\sin\varphi - y_{\mathrm{p}})\boldsymbol{j} + (z - z_{\mathrm{p}})\boldsymbol{k}], \quad (36)$$

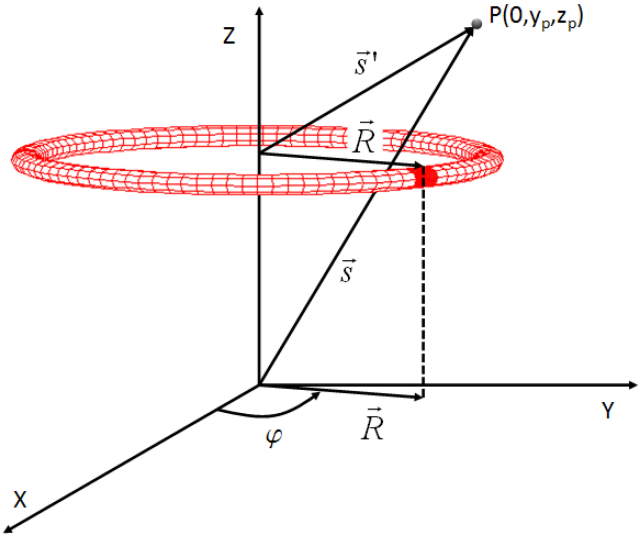

Figure 2. Sketch of the coordinate system and notation used to describe gravity.

where the meaning of the symbols is that shown in Fig. 2. The gravitational force acting on to the *i*-particle can be easily written as:

$$\boldsymbol{g_i} = \sum_{j=1}^{N} \frac{G}{2\pi} \frac{m_j}{\left(R_j^2 + s_i'^2\right)^{3/2}} \times[(R_j I_1 - y_i I_2)\boldsymbol{j} + (z_j - z_i) I_2)\boldsymbol{k}], \tag{37}$$

where ${s'}_i^2 = y_i^2 + (z_j - z_i)^2$, and $m_j = 2\pi R_j \rho_j$ is the mass of the particle associated to the *j*-ring. Integrals I_1 and I_2 are defined as follows:

$$I_1 = \int_0^{2\pi} \frac{\sin\varphi d\varphi}{(1 - \tau \sin\varphi)^{3/2}} \tag{38}$$

$$I_2 = \int_0^{2\pi} \frac{\mathrm{d}\varphi}{(1 - \tau \sin\varphi)^{3/2}}, \tag{39}$$

where the parameter τ is

$$\tau = \frac{2 y_i R_j}{R_j^2 + s_i'^2}. \tag{40}$$

Although the elliptical integrals I_1 and I_2 cannot be solved analytically, they can be tabulated as a function of the parameter τ given by equation (40). It is straightforward to show that the value of τ is always inside the interval $\tau \epsilon$ [0, 1), although for $\tau \to 1$ the integrals I_1 and I_2 become divergent. Therefore, the gravity force can be calculated in an efficient way using the following recipe.

(1) Build a table for I_1 and I_2 as a function of τ. A table with 10^4 rows with values $0 \leq \tau \leq 0.9999$ evenly spaced is sufficient.

(2) To increase the speed do not interpolate from that table but take just the row which is closest to the actual value of τ calculated using equation (40).

(3) Note that parameter τ is symmetric with respect any pair of particles, $\tau_i = \tau_j$, thus $I_1(\tau_i) = I_1(\tau_j)$ and $I_2(\tau_i) = I_2(\tau_j)$. Therefore, only half of the interactions have to be calculated.

If the algorithm is optimized the scheme is able to provide the exact value of the gravity for several dozens of thousand particles. In many applications, using $\simeq 5\ 10^4$ particles in two dimensions is enough to guarantee a good resolution.

Another physical magnitude of interest is the gravitational potential at the position of the *i*-particle. It is easy to show that the contribution of the *j*-ring to the gravitational potential is

$$V_i = \frac{G}{2\pi} \frac{m_j}{\left(R_j^2 + s_i'^2\right)^{1/2}} I_3, \tag{41}$$

where

$$I_3 = \int_0^{2\pi} \frac{\mathrm{d}\varphi}{(1 - \tau \sin\varphi)^{1/2}}. \tag{42}$$

Again the same recipe given above to compute the force can be used to efficiently calculate V_i. On the other hand, the exact computation of the gravitational potential allows to calculate the gravitational force by taking the gradient of *V* at any point.

$$\boldsymbol{g_i} = -(\boldsymbol{D}V)_i. \tag{43}$$

A more suitable form for SPH calculations can be obtained using

$$\widehat{\eta}\boldsymbol{D}V = \boldsymbol{D}(\widehat{\eta V}) - V\boldsymbol{D}\widehat{\eta}, \tag{44}$$

which, according to equations (7) and (9), leads to the following discrete equation:

$$\boldsymbol{g_i} = -(\boldsymbol{D}V)_i = \frac{f_1^i}{\widehat{\eta}_i} \sum_{j=1}^{N} m_j (V_i - V_j)\boldsymbol{D}_i W_{ij} + \frac{\left(\frac{\mathrm{d}f_1^i}{\mathrm{d}r}\right)}{\widehat{\eta}_i} \sum_{j=1}^{N} m_j (V_i - V_j) W_{ij} \boldsymbol{u}_r, \tag{45}$$

where f_1 is the corrective term given by equation (5) and u_r the unit vector in the *r*-axis.

This second route to calculate the gravitational force is computationally more efficient than evaluating equation (37) because the gradient of the potential is a local quantity which can be calculated in the same part of the algorithm devised to compute the density or other magnitudes in the hydrocode. It has the additional advantage that the resulting force is smoothed by the SPH interpolation procedure avoiding divergences when a pair of particles become too close. In Fig. 5 (bottom right-hand side), there are shown the gravity profile calculated using equation (45) (filled triangles) and the pressure gradient term (continuum line) along a Sun-like polytropic structure. As it can be seen, the fit is satisfactory except at the surface where the pressure gradient is overestimated. Although using the potential to calculate gravity is not as exact as the direct force calculation, it is a factor of 2 faster because there is a lesser amount of numerical operations in the double loop of the gravity routine.

Needless to say, the simplicity of the proposed scheme makes the parallelization of the gravity computational module straightforward. In this case, calculations with 10^5–10^6 particles could become feasible even for desktop computers with multiple core processors.

3.3.1 Free-fall collapse of homogeneous gas structures. Rotation

As an initial check of the gravity algorithm resulting from equation (45), we have simulated the free-fall collapse of a uniform density sphere of mass M_0 and radius R_0. It is a standard test which has the following analytical solution:

$$\frac{t}{t_{ff}} = 1 - \frac{2}{\pi}\left\{\sin^{-1}\left[\left(\frac{r}{r_0}\right)^{1/2}\right] - \left(\frac{r}{r_0}\right)^{1/2}\left(1 - \frac{r}{r_0}\right)^{1/2}\right\}, \tag{46}$$

where r_0 is the initial position of the fluid element and $0 \leq t \leq t_{ff}$. The free-fall time t_{ff} is

$$t_{ff} = \frac{\pi}{2}\left(\frac{R_0^3}{2GM_0}\right)^{1/2}. \tag{47}$$

We built an uniform sphere with $M_0 = 1\,\mathrm{M}_\odot$ and $R_0 = \mathrm{R}_\odot$ filled with $N = 15\,396$ particles settled in a square lattice. Gas pressure and artificial viscosity were set to zero so that the structure collapsed under gravity force. Afterwards the implosion was followed until the elapsed time was close to t_{ff}. Although restricted to spherical symmetry, the free-fall test is quite demanding because the evolution is highly non-linear, allowing for a good check of both the gravity module and the integration scheme (see next section for details). In Fig. 3, there is represented the evolution of a particle initially located at $r_0 = 2/3\,\mathrm{R}_\odot$. As we can see, its evolution is in good agreement to the analytical solution given by equation (46).

A question of great interest in astrophysics is the capability of axisymmetric SPH codes to handle rotation. The topic is far from

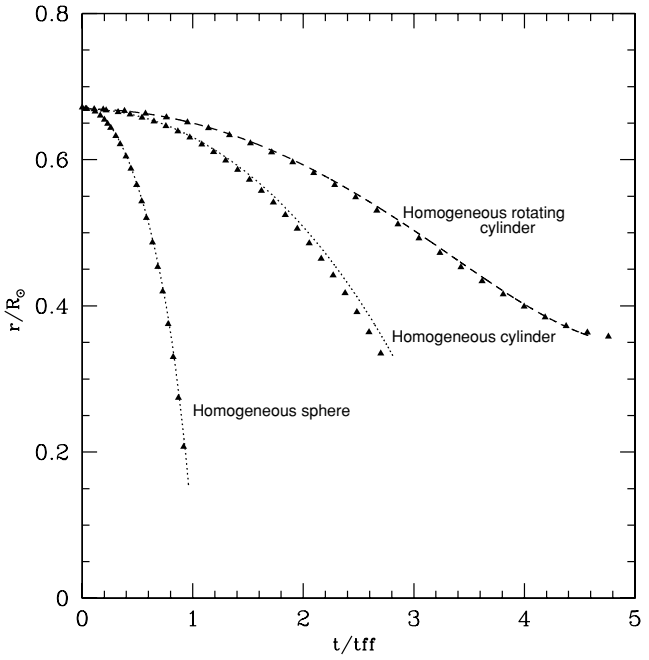

Figure 3. Free-fall test. Triangles represent the analytical solution in each case. The initial radius of the particle was $r_0 = 2/3\,\mathrm{R}_\odot$, $z_0 = 0$ in all cases.

trivial because in general it involves transport of angular momentum via viscous coupling. Even though a complete answer to that question is beyond the scope of the present work, there is a particular case that can be handled with the present scheme: the fast implosion (or expansion) of a self-gravitating rotating cloud. If the characteristic dynamical time is much shorter than the viscous coupling time we can impose angular momentum conservation around the symmetry axis to solve this problem. The strategy is simply to add the centrifugal force which arises from finite angular momentum to the r-component of gravity. As an example, we have simulated the collapse of a slender rotating cylinder of gas with uniform density centred at the coordinate origin. The initial conditions are specified by the mass $M_{\rm cyl}$, the radius $R_{\rm cyl}$ and the length of the cylinder $Z_{\rm cyl}$. If we suppose *rigid* rotation the specific angular momentum of a mass point is given by $L_z(r_0) = w_0 r_0^2$ being w_0 the initial angular velocity of the cylinder and r_0 the position of the fluid element at the initial time t_0. Angular momentum conservation demands $L_z(r, t) = L_z(r_0)$ so that the centrifugal force is $F_{\rm c} = L_z^2(r_0)/r^3(t)$ which is added to the first component of gravity, calculated using equation (45), to obtain an effective gravity value. As in the case of the spherical collapse, we have taken $M_{\rm cyl} = \mathrm{M}_\odot$ and $R_{\rm cyl} = \mathrm{R}_\odot$ while the cylinder length was $Z_{\rm cyl} = 20R_{\rm cyl}$. The evolution of mass points was followed assuming two values for the angular momentum: (1) zero angular momentum and (2) $L_z(r_0) = \sqrt{(0.5 g_0 r_0^3)}$, where $r_0 = 2/3R_{\rm cyl}$ for which centrifugal force was a half of gravitational force at that position. In this case, we have used a larger number of particles, $N = 70\,000$ to reduce boundary effects.

On the other hand, assuming $Z_{\rm cyl} >> R_{\rm cyl}$ and using the Gauss law it is possible to work out an analytical approach to the above scenario. The acceleration equation becomes

$$\ddot{r} = -g_0 \frac{r_0}{r} + \frac{L_0^2}{r^3}, \tag{48}$$

where $L_0 \equiv L_z(r_0)$ and g_0 is the value of gravity at $r = r_0$. According to the Gauss law, $g_0 = 2GM_{\rm cyl}\ r_0/(R_{\rm cyl}^2 Z_{\rm cyl})$, but it is better to take g_0 directly from the SPH simulation to ensure identical initial conditions in both calculations. The solution of equation (48) is

$$t(r) = -\int_{r_0}^{r} \frac{\mathrm{d}r'}{\left[-2g_0 r_0 \ln(r'/r_0) + L_0^2\left(\frac{1}{r_0^2} - \frac{1}{r'^2}\right)\right]^{1/2}}, \tag{49}$$

which has to be solved numerically once r_0 and L_0 are specified.

Fig. 3 depicts the evolution of a particle initially located at $r_0 = 2/3R_{\rm cyl}$, $Z_0 \simeq 0$ without and with initial angular momentum as well as that obtained using the analytical approach, equation (49). The case with zero angular momentum led to the free fall of the mass element which was less violent than the spherical case owing to the lower initial density in the cylinder. As it can be seen in Fig. 3, the agreement between analytical and SPH results is not as good as in the spherical case for $t > t_{ff}$. This is not surprising because boundary effects at cylinder edges progressively affect gravity at current particle test position and its evolution is very sensible to small variations of gravity force.

When angular momentum was added to the cylinder at $t_0 = 0\,\mathrm{s}$, the implosion of the structure slowed down. As commented above, the amount of angular momentum was chosen to get a centrifugal force contribution at $r_0 = 2/3R_{\rm cyl}$ equals to a half of gravity force at that position. As we can see in Fig. 3, the result of the simulation is in better agreement to the analytical approach than the pure free-fall case. This is because the evolution is driven not only by gravity and errors due to the finite size of the rotating cylinder are not affecting so much the outcome as in the non-rotating case. At $t \simeq 5\mathrm{t}_{ff,}$ the fluid element begins to be centrifugally sustained, in good match to the analytical estimation.

4 TEST CASES

In this section, we describe and discuss in detail five test cases addressed to validate the computational scheme developed in the precedent sections. The first test involves the propagation of a thermal discontinuity born at the symmetry axis. It is a well-known calculation which has an analytical solution to compare with. Three calculations: the gravitational collapse of a polytrope, the implosion of a homogeneous capsule, and the wall shock problem deal with implosions of spherically symmetric systems. Although, at first glance, such constraint looks too restrictive in fact it is not because the spherical symmetry is not a natural geometry for axisymmetrical systems described with cylindrical coordinates. Any deviation from the pure spherical symmetry during the implosion will trigger the growth of hydrodynamical instabilities. Therefore, the preservation of the symmetry during the calculation is an important feature to be added to mass, momentum and energy conservation. Finally, the last test was devoted to simulate the collision of two bubbles of fluid along the Z-axis.

The initial models were calculated by mapping the spherically symmetric profiles into a two-dimensional distribution of particles settled in a square lattice. The mass of the particles was conveniently adjusted to reproduce the density profile of the one-dimensional model. For example, masses proportional to the r-coordinate of the particle were taken to obtain models with constant density. Reflective boundary conditions using specular ghosts particles were imposed across the Z-axis. The EOS was that of an ideal gas with $\gamma = 5/3$ and radiation in the test devoted to the collapse of a polytrope, and only gas ideal for the other tests. We have used and adaptive smoothing length parameter $h(\boldsymbol{s}, t)$ which was updated at each time-step to keep a constant number of neighbours $n_v = 36$ within a circle of radius $2h$. The interpolating kernel was the cubic polynomial spline. Numerical integration of SPH fluid equations was performed

using a two-step centred scheme with second order accuracy. It is worth to mention that in the free-fall test of a homogeneous sphere the velocity was updated using the XSPH (where X stands for any generic filtered variable) variant of Monaghan (1989) to avoid particle penetration through the symmetry axis. In this particular test, mass points at low radius are proner to cross Z-axis because pressure and viscous forces were artificially set to zero. Therefore, any residual value of gravity can impel particles located close to the centre towards unphysical $r < 0$ values. We have updated only the r-component of velocity using the following expression:

$$\tilde{\dot{r}}_i = \dot{r}_i + \epsilon 2\pi r_i \sum_{j=1}^{N} \frac{m_j}{\widehat{\eta}_{ij}} (\dot{r}_j - \dot{r}_i) W_{ij}, \tag{50}$$

where $\tilde{\dot{r}}_i$ is the new, smoother, velocity. The parameter ϵ was taken variable,

$$\epsilon = \begin{cases} \epsilon_0 \left[1 - \frac{(r/h)^2}{9}\right] & r \leq 3h \\ 0 & r > 3h \end{cases} \tag{51}$$

where $\epsilon_0 = 0.5$. Using XSPH variant to move particles enforces $\dot{r} \to 0$ when $r \to 0$, making it difficult for particles to cross the axis.

4.1 Evolution of a thermal discontinuity

Lets consider the problem relative to the propagation of a thermal wave moving through an uniform static medium. This is a well-known test, addressed to check the capability of the numerical scheme to handle thermal discontinuities. The initial model was a sample of 57 908 particles evenly distributed in a square lattice so that the density was $\rho = 1\,\mathrm{g\,cm^{-3}}$. A δ-like jump in internal energy originates a thermal wave front which evolves according to

$$u(r, z, t) = \frac{A}{(4\pi c_v k t)^{3/2}} \exp\left(-\frac{r^2 + z^2}{4 c_v k t}\right) + u_0, \tag{52}$$

where c_v is the specific heat and k is the thermal conductivity. The following set of values were taken $A = 10^5\,\mathrm{erg\,cm^3\,g^{-1}}$, $u_0 = 10^3\,\mathrm{erg\,g^{-1}}$ and $c_v k = 1\,\mathrm{cm^2\,s^{-1}}$. The initial internal energy profile was that given by equation (52) for $t = 1$ s, which was taken as the initial time ($t = 0$ s) for the SPH simulation. The evolution of the thermal signal is then controlled by the heat conduction equation, equation (35).

In Fig. 4 (left-hand side), there is represented the thermal profile at different times. As we can see the coincidence with the analytical solution given by equation (52) is excellent. As time goes on the peak of the signal and its slope decreases due to heat diffusion. The initial discontinuity is rapidly smeared out by thermal diffusion and soon a thermal wave is born which travels to the right, equalizing the internal energy of the system. At $t = 5$ s, the profile of the internal energy of the gas is already quite flat and the system is not far from thermal equilibrium. At that moment, total energy was conserved up to 5×10^{-5}. In Fig. 4 (right-hand side), it is shown the evolution of the thermal profile which results when the first term on the right-hand side in equation (35) is removed. As we can see, the evolution is no longer reproduced by the SPH calculation. Therefore, it is of utmost importance to include that term, especially in those calculations dealing with strong thermal gradients close to the symmetry axis.

4.2 Gravitational collapse of a polytrope

The second test involves a catastrophic, albeit highly unprobable, astrophysical scenario. A spherically symmetric Sun-like polytrope was suddenly unstabilized by removing the 20 per cent of its internal energy so that the structure collapsed under the gravity force. At some point, the collapse is halted and an accretion shock forms which manages to eject part of the mass of the polytrope. Several episodes of recontraction followed by mass loss ensued until the star sets in a new equilibrium state. Even though that particular scenario is not realistic, it contains several pieces of physics of great interest because accretion shocks and pulsational instabilities are ubiquitous in astrophysics. As the initial model has spherical symmetry, we expect it to be preserved during the implosion and further bounce. The conservation of the symmetry is a demanding test for multidimensional hydrocodes in those cases where there are episodes of strong decelerations. In the particular case of axisymmetric hydrodynamics, the higher numerical noise close to the symmetry axis may trigger the growth of convective instabilities. An additional advantage of considering an spherically symmetric initial model is that the evolution calculated with the SPH code

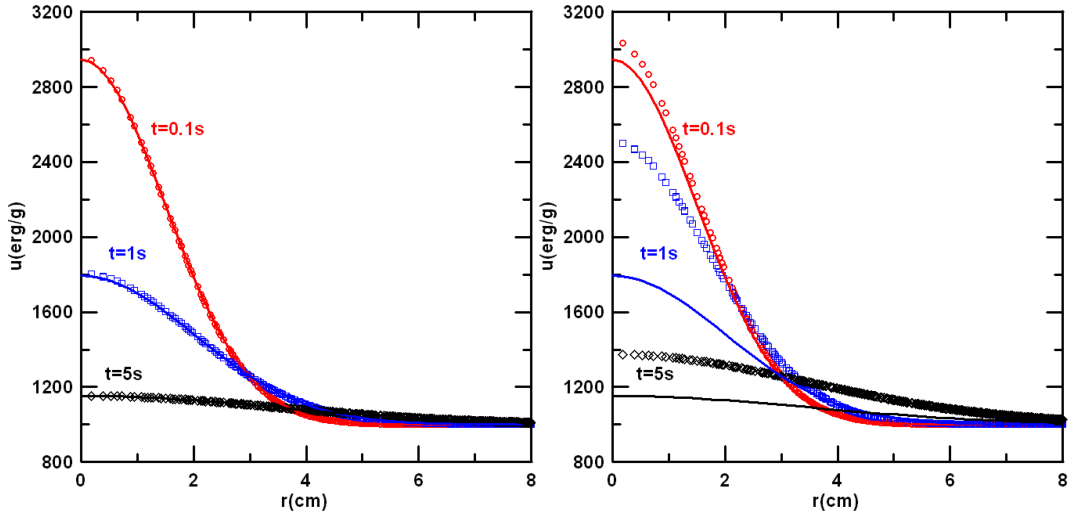

Figure 4. Evolution of a thermal discontinuity initially seeded around the symmetry axis. The profile of the internal energy at different times is well reproduced by the SPH when the hoop-stress term is included (left-hand side). However, when that term is neglected the result does not match the analytical solution represented by the continuum line (right-hand side).

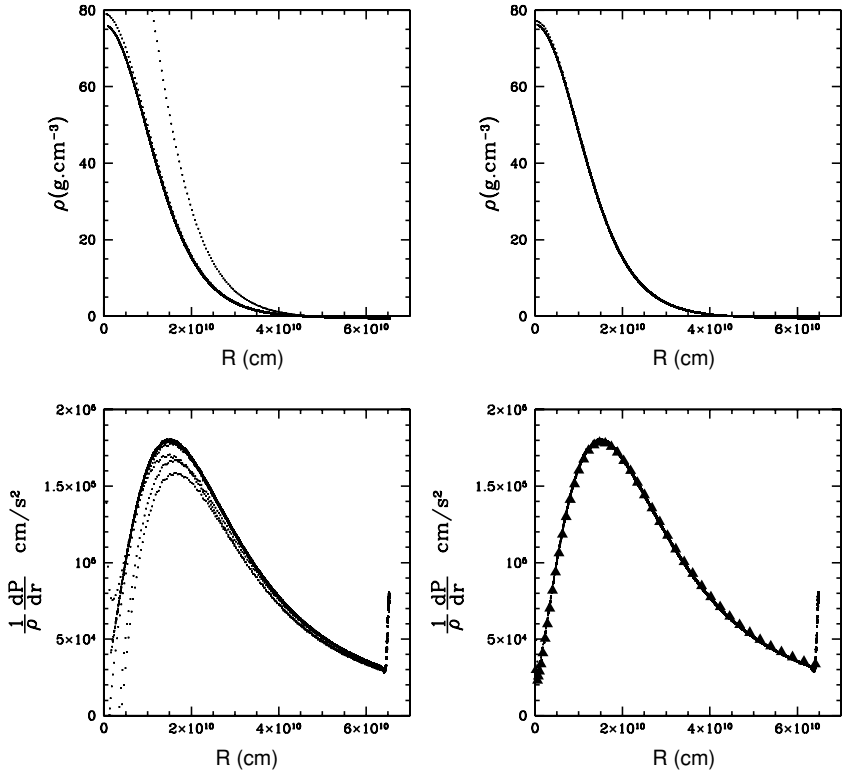

Figure 5. Density, gravity and pressure gradient profiles of the polytrope. Upper left- and right-hand side: density profile without and with axis corrections, respectively. Bottom left- and right-hand side: the same but for the pressure gradient. The absolute value of gravity computed using the gradient of the gravitational potential calculated using equation (45) is marked with full triangles (bottom right-hand side). All mass points of the polytrope have been represented. Neglecting axis corrections leads to a much larger dispersion in the profiles.

can be checked using standard Lagrangian hydrodynamics in one dimension.

The initial model was a $1\,M_\odot$ spherically symmetric polytrope of index $n = 3$. The radius was set equal to $1\,R_\odot$ so that the central density was $\rho_c = 77\,g\,cm^{-3}$. Once the one-dimensional equilibrium model was built, it was mapped to a two-dimensional distribution of 51 408 particles located in a rectangular lattice. The mass of the particles was conveniently adjusted to reproduce the density profile of the polytrope. In Fig. 5, there are shown the profiles of density and gradient of pressure at $t = 0$ s calculated using the two-dimensional SPH. As we can see, the inclusion of the corrective term f_1 given by equation (5) in the momentum equation is crucial to get good enough profiles of these quantities to guarantee the stability of the initial model. The polytrope was perturbed by reducing the temperature everywhere in a 20 per cent of its equilibrium value. Afterwards, the evolution was followed with the two-dimensional SPH from the implosion until the first pulsation and compared to that obtained by a one-dimensional Lagrangian hydrocode. The main features of the model and a summary of the results are shown in Table 1.

Soon after the model was destabilized, the polytrope started to collapse. At $t = 960$ s, a maximum of the central density $\rho_{max} = 192.8\,g\,cm^{-3}$ was reached. A similar maximum of $\rho_{max} = 187.1\,g\,cm^{-3}$ was obtained using one-dimensional hydrodynamics. The profiles of density and radial velocity at different times are depicted in Fig. 6. As we can see, the evolution calculated in one and two dimensions is very similar and, in general, both profiles are in good agreement. At our last calculated time, $t = 1545$ s, the shock is already breaking out the surface of the polytrope. Shortly after that time, some mass is ejected from the surface and, as the one-dimensional calculation shows, the star embarks in a long pulsational stage until a new equilibrium state is achieved.

Therefore, the numerical scheme was able to handle with this scenario. The algorithm devised to calculate the gravity using equation (45), which relies in the direct interaction between rings (Fig. 2),

Table 1. Main features of test models described in Sections 4.2 and 4.3. Conservation of momentum is given by the centre of mass displacement $\Delta\bar{r} = [(\bar{r}(t) - \bar{r}_0) - \bar{v}_r^0 t]$ and $\Delta\bar{z} = [(\bar{z}(t) - \bar{z}_0) - \bar{v}_z^0 t]$ divided by the radius of the configuration at that time (Columns 5 and 6). Momentum and energy conservation correspond to the last calculated model shown in Figs 6–9.

Test	Number of particles	$\left(\frac{\rho_{max}}{\rho_0}\right)_{1D}$ [a]	$\left(\frac{\rho_{max}}{\rho_0}\right)_{2D}$	$\frac{\lvert\Delta\bar{r}\rvert}{R}$	$\frac{\lvert\Delta\bar{z}\rvert}{R}$	$\frac{\lvert\Delta E\rvert}{E_0}$
Polytrope	51 408	2.43	2.49	5×10^{-15}	10^{-11}	5×10^{-3}
Capsule implosion	30 448	29	32	4×10^{-14}	10^{-11}	$8\,10^{-3}$
Noh test	50 334	64	58	6×10^{-14}	3×10^{-8}	2×10^{-3}
Gas clouds collision	55 814	–	–	5×10^{-14}	1.3×10^{-3}	10^{-2}

[a] Analytical value for the Noh test.

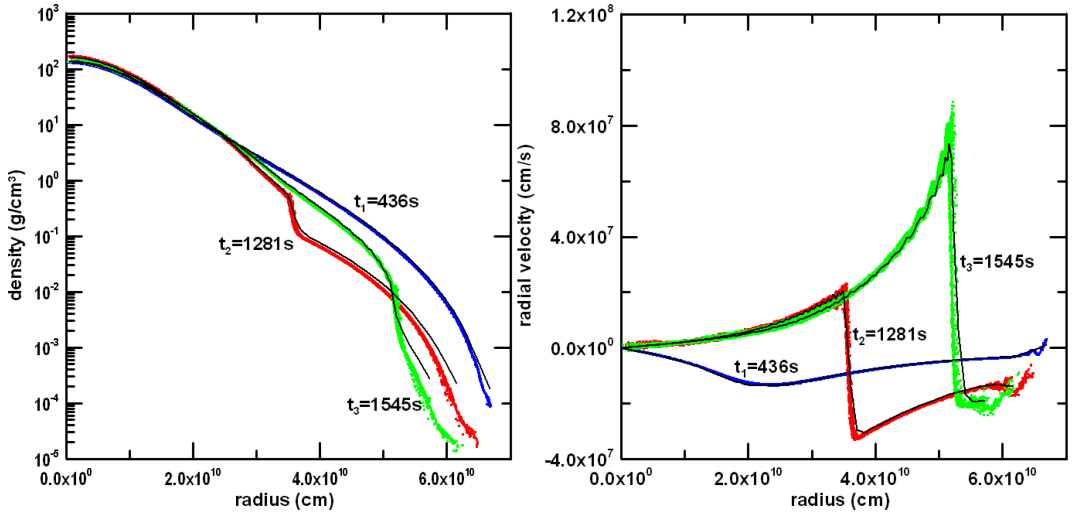

Figure 6. Density profile (left-hand side) and radial velocity (right-hand side) during the implosion and further rebound of the polytrope at different times. The black continuum line is the profile calculated using a one-dimensional hydrocode of similar resolution. At $t = 1545$ s, the shock wave is breaking the surface of the star. In the figure, all particles used during the calculation are shown.

did a good job. The artificial viscosity module was also able to keep track with the shocks although, at some stages, the post-shock region showed a small amount of spurious oscillations. These numerical oscillations in the velocity profile are clearly visible in Fig. 6 at $t = 1545$ s. In the last three columns of Table 1, there is information concerning momentum and energy conservation at $t = 1545$ s, our last calculated model. There was an excellent momentum conservation, close to machine precision, whereas the conservation of energy was more modest, $\simeq$0.5 per cent. On the other hand, the spherical symmetry was also quite well preserved during the calculation. On the negative side, we find that the two-dimensional calculation was systematically delayed with respect to its one-dimensional counterpart. The relative shift in time remained approximately constant, around 1.5 per cent, during the evolution. For the sake of clarity, the elapsed times shown in Fig. 6 were that of the SPH simulation and the times of the one-dimensional evolution were conveniently chosen to fit the two-dimensional profiles.

4.3 Implosion of a homogeneous capsule

Probably the most unfavourable case to numerical simulation is that of a strong implosion as it currently appears, for example, in ICF studies. Thus, our third test deals with the implosion of a homogeneous spherical capsule of size $R_0 = 1$ cm and density $\rho_0 = 1\,\mathrm{g\,cm^{-3}}$, induced by the (artificial) ablation of its surface. The ablation of the capsule was triggered by the instantaneous deposition of energy in the outermost layers of the capsule, which had their internal energy increased in the same proportion. The energy deposition profile was taken linear from $s = 0.8$ to $s = R_0 = 1$ cm so that the internal energy at $R_0 = 1$ cm was a factor of 10^4 higher than that at $s = 0.8$ cm. Below $s = 0.8$ cm a flat profile of the internal energy was assumed. The rocket effect caused by the evaporation of the surface layers forms a strong shock wave which compresses the interior of the capsule. The convergence of the shock at the centre of the sphere increases the temperature and the density in a large factor, much larger than that obtained in the previous section dealing with the collapse of a solar-like polytrope. The main features of the model are shown in Table 1 and Fig. 7. The profiles of density and radial velocity at several times are depicted in Fig. 7 which also shows the profiles obtained using a one-dimensional Lagrangian hydrocode (continuum lines) with the same physics and identical initial conditions. The evolution of the capsule can be summarized as follows. Soon after the initial energy deposition a pair of shock waves moving in opposite directions appear (profiles at $t = 0.0044$ s in Fig. 7). As the reverse shock approaches the centre, it becomes stronger owing to the spherical convergence (profiles at $t = 0.0087$ s in Fig. 7). Once the maximum compression point is reached, $\rho_{\max} = 32\,\mathrm{g\,cm^{-3}}$ at $t = 0.0111$ s, the wave reflects. When $t = 0.0150$ s, the density peak has already dropped to $7\,\mathrm{g\,cm^{-3}}$ and most of the material of the capsule is expanding homologously. At $t = 0.0264$ s, the reflected wave reaches the initial radius of the capsule, $R_0 = 1$ cm. At that time, the material of the capsule is rather diluted $\rho(r) \ll 1\,\mathrm{g\,cm^{-3}}$ and the radial velocity profile consist of two homologously expanding zones separated by a transition region at $s \simeq 1$ cm. At the last calculated time, $t = 0.0264$ s, the outermost layer of the sphere has expanded until $s = 10$ cm, 10 times the original size of the capsule. As we can see, the two-dimensional simulation matches quite well the one-dimensional results. According to Table 1, the central density at the moment of maximum compression is almost the same in both calculations. The conservation of momentum is very good, close to machine precision (Columns 5 and 6 of Table 1), while numerical energy losses remained lesser than 1 per cent (last column in Table 1). However, an inspection of Fig. 7 reveals that the spherical symmetry was not so well preserved as in the collapsing polytrope. Now the implosion of the capsule was more violent and the deceleration phase before the bounce was more intense, making easier the growth of instabilities. Even though the initial model had good spherical symmetry, the initial distribution of the particles in a regular lattice acts as a source of the so called hour-glass instability. Such instability is related to the existence of preferred directions along the grid through which the stress propagates. As in the previous test, another point of conflict between the one-dimensional and the two-dimensional calculations is that the two-dimensional evolution is a bit delayed with respect its one-dimensional counterpart. For instance, the times at which the maximum central densities are achieved are $t_{1D} = 0.01\,095$ s and $t_{2D} = 0.0111$ s, so that the relative difference was around

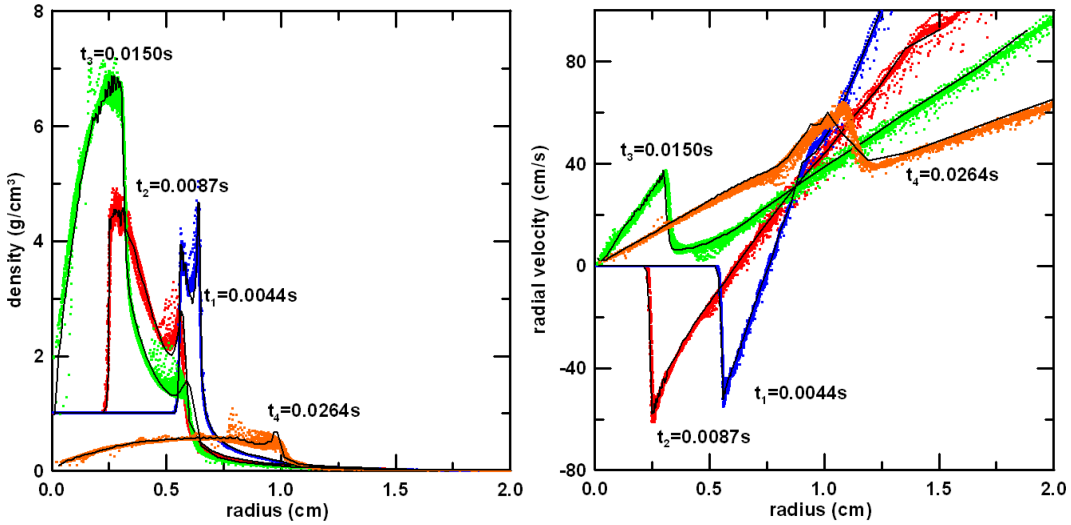

Figure 7. Same as in Fig. 6 but for the small capsule implosion.

1–2 per cent. Such percent level of discrepancy remained approximately constant during the calculation.

4.4 Wall heating shock: the Noh test

The wall heating shock test, Noh (1987), was especially devised to analyse the performance of algorithms addressed to capture strong shocks. Basically, the wall heating shock test consists in making a sphere or a cylinder implode by imposing a converging velocity field. For these geometries, there is an analytical approach to the evolution of density and thermodynamical variables as a function of the initial conditions. The results of numerical codes can be compared with the analytical solution to seek the best method or to choose for optimal combination of parameters. It is well known that schemes which rely in artificial viscosity have difficulties to handle the wall heating shock test. The reason is that artificial viscosity spreads the shock over a three or four computational cells, which induces an unphysical rise of internal energy ahead the shock. In the case of spherical or cylindrical geometry, the artificial increase in internal energy is magnified by the geometrical convergence of the shock. Therefore, the wall shock problem represents a strong challenge for the axisymmetric SPH. Brookshaw (2003) carried out a similar test with the SPH code but far from the symmetry axis. In particular, he modelled the impact of two supersonic streams of gas, obtaining good profiles for density and internal energy except in a small region around the collision line. The density profile showed a dip at that region while a large spike was seen in the internal energy. Both, the dip and the spike were numerical artefacts which can be smoothed out by using an artificial heat conduction term to spread the excess of internal energy and reduce the error around the contact discontinuity.

To check the performance of our code, we have settled $N = 50\,334$ particles in a square lattice. As in the previous tests, the mass of the particles was conveniently crafted to reproduce an spherical homogeneous system with initial radius $R_0 = 1$ cm. The initial conditions were taken as in Noh (1987): $\rho(s, 0) = 1\,\mathrm{g\,cm^{-3}}$; $\dot{s}(s, 0) = -1\,\mathrm{cm\,s^{-1}}$; $u(s, 0) = 0\,\mathrm{erg\,g^{-1}}$. The exact solution at time $t = 0.6$ s for $\gamma = 5/3$ is shown in Fig. 8 (dashed line). The analytical profile is characterized by a constant post-shock state until distance $s = 0.2$ cm followed by a rapid decrease in density and internal energy. In the shocked zone density reach a constant value $\rho = 64\,\mathrm{g\,cm^{-3}}$ while internal energy was $u = 0.5\,\mathrm{erg\,g^{-1}}$. The combination of such harsh initial conditions plus geometrical convergence leads to a strong implosion, even harder than that described in the ablated capsule test. In Fig. 8 (left-hand side), there are shown the spherically averaged profiles of density and internal energy obtained using SPH at $t = 0.6$ s. The error bars in the plot give the 1σ dispersion of these variables with respect to its mean value in the shell. As we can see, the resulting profiles compare poorly with the analytical results in the shocked region. In addition, the dispersion is high, especially at low radius, a clear signature for the presence of numerical noise. Close to the axis there is the typical artificial combination of a dip (in density) and spike (in internal energy). The maximum density value was $\rho \simeq 58$ which is around 10 per cent lower than the exact value. Such bad quantitative agreement was not unexpected because it is common to all hydrodynamic codes which use the artificial viscosity scheme. A way to improve the quality of the simulation is to allow for heat conduction in the hydrocode to remove the thermal energy spike and to sharpen the shock. Recipes to obtain an artificial conductivity coefficient in SPH to better handle the wall shock problem were given by Monaghan (1992) and Brookshaw (2003). For this calculation, we have adapted the recipe of Monaghan to the features of the axisymmetric SPH defining an artificial conductivity for the i-particle,

$$k_i = \bar{\rho}_{ij}\bar{c}_{v_{ij}}\bar{h}_{ij}(\bar{c}_{ij} + 4|\mu_{ij}|), \tag{53}$$

where $\bar{c}_{v_{ij}}$ is the symmetrized specific heat and $|\mu_{ij}|$ is the artificial viscosity parameter given by equation (24). According to equation (53) $k_i = k_j$, which can be used directly in equation (35) to compute the artificial heat flux. As shown in Fig. 8 (right-hand side), the inclusion of the artificial heat conduction term leads to a significant improvement of the results. Not only the profound dip in density in the central region has been removed but also the simulation shows much lesser dispersion around the averaged values of density and internal energy. However, the maximum peak in density still remains $\simeq$10 per cent below the theoretical value. In this respect, the only way to improve the results is sharpening the shock either by using adaptive kernels, Owen et al. (1998), Cabezón, García-Senz & Relaño (2008), or by increasing the number of particles.

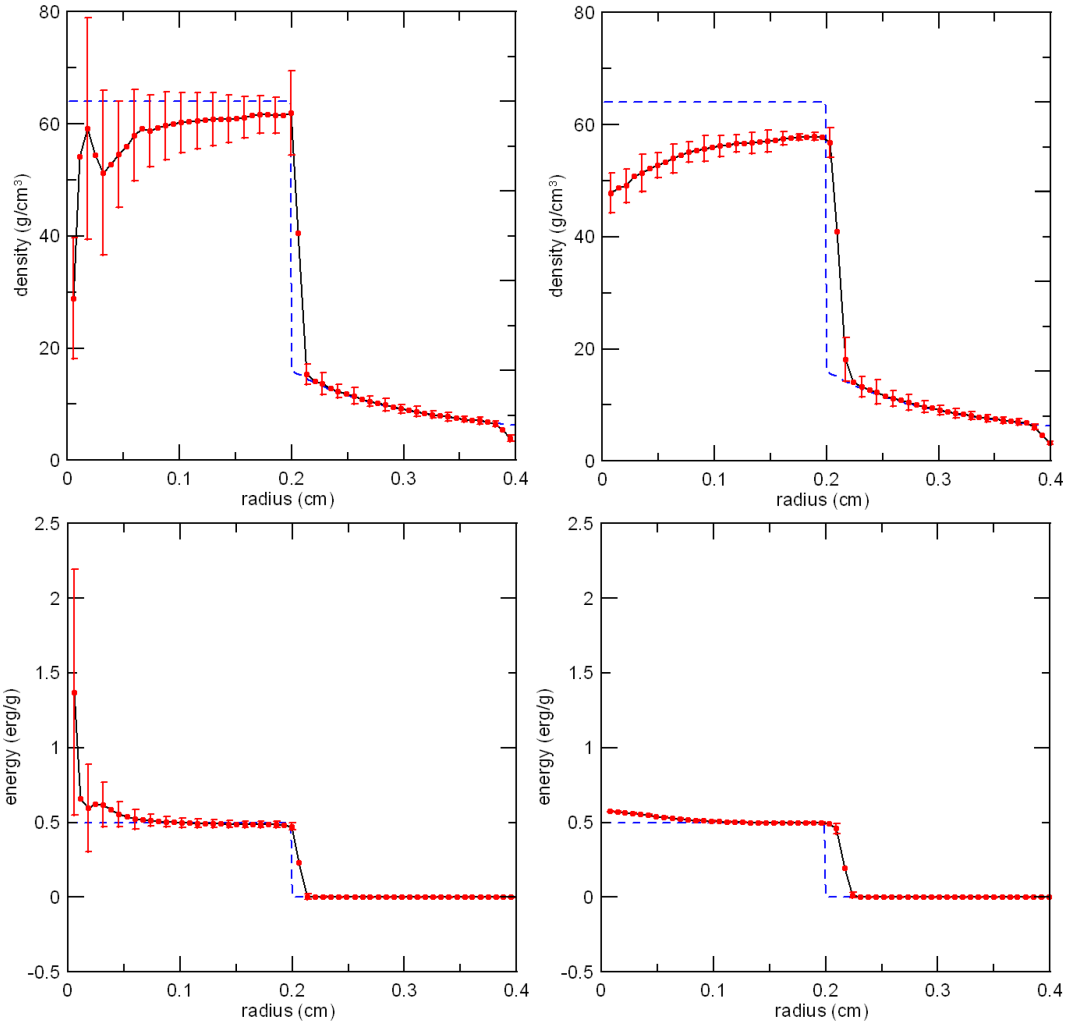

Figure 8. Results of the Noh test at $t = 0.6$ s. Upper left- and right-hand side: averaged density profiles without and with the artificial heat conduction. Bottom left- and right-hand side: same but for internal energy. Dispersion around the averaged values are given by the error bars.

4.5 Supersonic collision of two streams of gas

Our last test is specifically addressed to check momentum conservation in a very anisotropic situation: the supersonic collision along the Z-axis of two homogeneous spherical clouds of gas with different size and mass. The size and mass of the spheres are $R_1 = 1$ cm; $M_1 = 4\pi/3$ g and $R_2 = 3$ cm; $M_2 = 36\pi$ g, respectively, so that their density is $\rho_1 = \rho_2 = 1\,\mathrm{g\,cm^{-3}}$. The biggest sphere is at rest with its centre located at (0, 0) cm while the smaller one is centred at (0, −5) cm moving upwards with velocity $v_z^0 = 10\,\mathrm{cm\,s^{-1}}$. The initial internal energy of both spheres was $u_1^0 = u_2^0 = 10^{-3}\,\mathrm{erg\,g^{-1}}$, whereas EOS obeys an ideal gas law with $\gamma = 5/3$. The corresponding initial Mach number was $M_s^0 \simeq 500$, thus the impact is supersonic. The number of particles in each sphere was $N_1 = 5480$ and $N_2 = 50\,334$, respectively.

In Fig. 9, there are represented several snapshots showing the density evolution during the collision process. As can be seen the large mass contrast leads to the complete deformation of the smaller sphere which, in the end transfers most of its initial momentum to the larger bubble. Information about the evolution of the centre of mass of each bubble as well as that of the whole system is provided in Fig. 10. According to Figs 9 and 10, the collision history can be roughly divided in three stages. (1) For $0 \leq t \leq 0.5$ s, the incoming smaller cloud deforms while a large fraction of its kinetic energy went into internal energy around the collision region. A shock wave was launched into the larger bubble, (2) between $0.5 \leq t \leq 1$ s, the total internal energy did not change so much. At $t = 1$ s, the velocity of the centre of mass of both structures was practically the same, (3) for $t > 1$ s, the energy stored as internal energy is again restored to the system. At large times, the velocity of the smaller bubble became negative while the bigger cloud acquired a positive velocity to preserve total momentum. At our last time $t = 1.4$ s, the interaction between both structures is coming to an end. Fig. 10 also shows that, in spite of the large changes in the velocity of each bubble, the velocity of the centre of mass of the whole system remained unaltered.

In the last row of Table 1, there are shown several magnitudes related to momentum and energy conservation. Conservation of linear momentum during the interaction was monitored through the displacement of the centre of mass of the system. At the final time, $t = 1.4$ s, the deviation of the centre of mass position with respect to the value expected from $\bar{v}_z^0 t$ was much larger than that shown in the other tests. Still the relative error in the position of the centre of mass once the collision has practically ceased was $\simeq 10^{-3}$. Angular

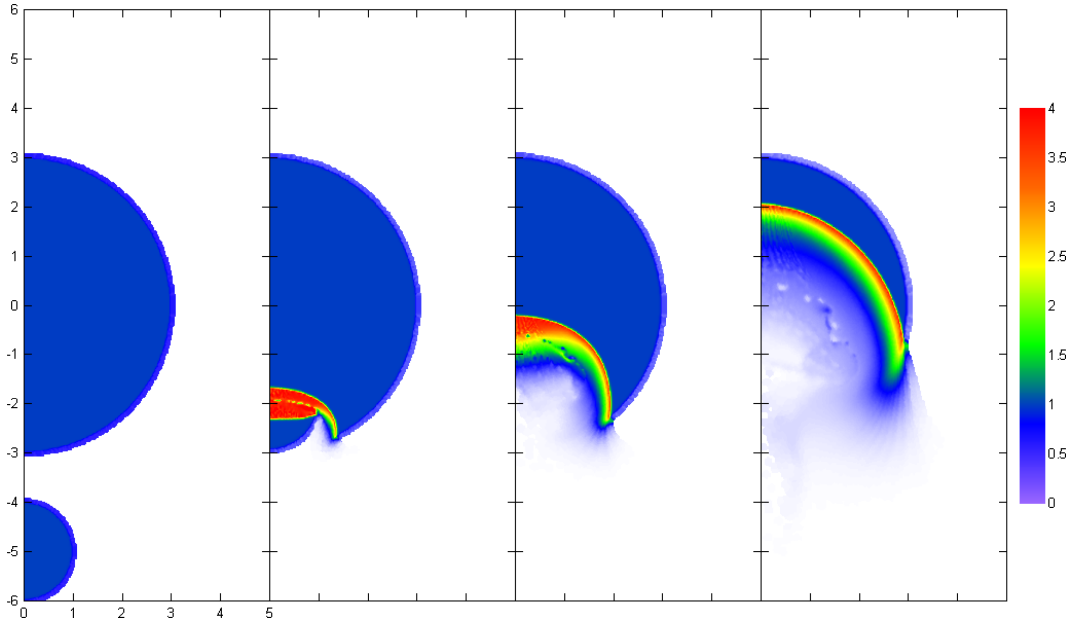

Figure 9. Density colour-map of the collision of two streams of gas at times $t = 0$, 0.31, 0.69 and 1.41 s. Axis units are in centimetres.

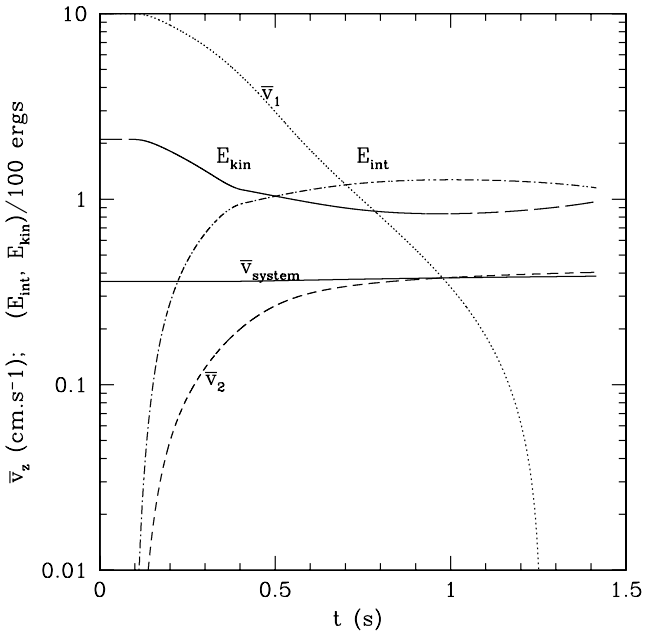

Figure 10. Evolution of $\bar{v}_z$ of the centre of mass of each bubble and of the system. Subscripts 1 and 2 refer to the smaller and larger bubble, respectively. Evolution of total kinetic and internal energy is also given.

momentum was very well preserved, almost to machine precision. Total energy was conserved to 10^{-2} relative to the initial kinetic energy of the system.

In an attempt to understand the origin of the discrepancy relative to momentum conservation in the Z-direction, we ran exactly the same model but this time symmetrizing equation (13) (multiplying the term $P_j r_j / \hat{\eta}_j^2$ by f_1^j). There was no significant changes. We conclude that strict total momentum conservation in the Z-direction was not possible because of the interaction between real and reflected particles. Such interaction took place in a small band around the symmetry axis, acting as an external force which modified momentum of real particles. However, that force cannot be balanced by an opposite force acting in the left semiplane because, in the Z-direction, reflected particles were obliged to move exactly in the same way real particles did. Therefore, if strong directional anisotropies appear in the vertical displacements of the mass points some degree of violation in momentum conservation is unavoidable. Eventually, momentum conservation should improve as the number of particles increase because the amount of mass settled in the axis vicinity is lower.

5 CONCLUSIONS

Despite the success of the SPH technique to handle gas-dynamics problems in three dimensions, little effort has been invested to develop two-dimensional (axisymmetric) applications. This work intends to fill that gap by solving many of the problems often invoked in connection with SPH in cylindric coordinates. These are the treatment of the singularity axis, the handling of shock and thermal waves and, in many astrophysical scenarios, an accurate procedure to calculate the gravitational force. Our general philosophy in developing the mathematical formalism was to remain as close as possible to the Cartesian scheme so that many of the results of the standard SPH in three dimensions can be extrapolated with minimum changes to the axisymmetric version.

Starting from the fluid Euler equations given by Brookshaw (2003), we have obtained analytical corrections to those particles which move close to the singularity axis. These corrections appear as multiplicative factors to the different terms of the fluid equations. Such multiplicative factors become equal to one when $r > 2h$ (Fig. 1) so that there is no need to calculate them beyond that distance and the method is computationally efficient. Once the basic formalism was built, we added several pieces of physics which make the scheme well suited to handle a large variety of problems. First of all an extension of the three-dimensional standard artificial viscosity to the two-dimensional axisymmetric realm was devised, equations (23)–(25). The artificial viscosity includes the

convergence of the flow towards the symmetry axis via linear and quadratic terms proportional to $[(v_r h)/r]$ (being r the distance to the symmetry axis). These terms arise because the diagonal part of the stress tensor in cylindric coordinates includes the divergence of the flow velocity. However, the Cartesian part of the divergence was already present in the standard formulation given by equations (22) and (23) giving rise to bulk and shear viscosity. Therefore, only the axis converging part of velocity divergence, proportional to v_r/r has been added. The resulting viscous force Π^{2D} has two terms: $\Pi^{(1)}$ (Cartesian) and $\Pi^{(2)}$ (axis converging part) which are calculated using similar expressions, equations (23) and (25) involving four constants α_0, β_0 $[\Pi^{(1)}]$ and α_1, β_1 $[\Pi^{(2)}]$. The axis converging part of viscosity will be of importance only for strong implosions. Although in the simulations reported in this paper, we have taken $\alpha_0 = \alpha_1 = 1$ and $\beta_0 = \beta_1 = 2$ there could be other plausible combinations worth to explore. A similar approach was used to built the conductive transport equation. Starting from the expression given by Brookshaw (1985), we have added a new term that accounts for the divergence of the temperature gradient in the axis neighbourhoods. Even though the resulting expression was not totally antisymmetric, it led to a satisfactory energy conservation in the tests described in Sections 4.1 and 4.4. Finally, the set of equations was completed with the inclusion of self-gravity. In axisymmetric geometry, it is better to rely in the direct, ring to ring, interaction to compute gravity. Such procedure, although in general computationally expensive, has several advantages: (1) it does not rely in any sort of grid and gives the exact value of the gravitational force, (2) the calculations are feasible for a moderate number of particles (i.e. around 5×10^4 in serial desktop machines) which often suffice in many two-dimensional simulations and (3) the scheme is clear and extremely simple making it straightforward to parallelize. The algorithm devised to compute gravity was able to keep track the free-fall collapse of an homogeneous sphere as well as of an homogeneous rotating cylinder. Given an initial amount of rotation, the evolution of any point of the cylinder was handled by imposing angular momentum conservation around the symmetry axis.

Five test cases aimed at validating the computational scheme were considered. Each of them intended to check a particular physics item: heat conduction (Sections 4.1 and 4.4), shock waves (Sections 4.3 and 4.4) and gravity (Sections 3.3.1 and 4.2). Momentum conservation was specially checked in Section 4.5. Because for the most part the initial configurations had spherical symmetry, the preservation of that symmetry during the collapse and further expansion of the system was taken as an indicator of the general ability of the scheme to handle large changes in the spatial scale. It was also possible to make detailed comparisons of the results with those obtained either from analytical calculations, as in the case of the thermal wave propagation, or from one-dimensional simulations carried out using standard Lagrangian hydrodynamics. The results, obtained using several dozen thousand particles, were in good agreement with the analytical expectations and to the one-dimensional simulations. Additionally, there was an almost perfect momentum conservation while numerical energy losses always remained lesser than 1 per cent. The spherical symmetry was well preserved although a slight deviation was observed in the capsule implosion test, partially due to the so called hour-glass instability (owing to the initial setting of the particles in a lattice) and, despite the corrective terms, to the effect introduced by the singularity axis on to the approaching particles. A similar but probably more demanding test was the wall heating shock problem, dealing to the spherically symmetric implosion of a supersonic stream of gas. Although the results are not as good as those obtained with other methods which do not use artificial viscosity, they are comparable with one-dimensional calculations with similar resolution relying in artificial viscosity schemes. However, the results improved when artificial heat conduction, calculated using equations (35) and (53), was switched on.

As discussed in Section 4.5, a weak point of the formulation is that the inclusion of reflective particles in the scheme could degrade total momentum conservation in the Z-direction. However, a good momentum conservation, much better than energy conservation for instance, is expected in those systems in which the velocity field is not too anisotropic. If strong momentum exchange along the Z-axis is expected, as in the test described in Section 4.5, then momentum will be preserved to a similar level as total energy.

As a conclusion, we can say that the formulation of the axisymmetric SPH given in this paper is a solid tool to carry out simulations using that particle method. However, there are still a number of unresolved issues which deserve further development. One of them is how to build good initial models without settling particles of different mass in regular lattices. This is important because ordered lattices introduce spurious instabilities in the system and the mixing of particles with very different masses could lead to numerical artefacts. Another point of difficulty has to do with artificial viscosity because it introduces too much shear viscosity in the system damping the natural development of hydrodynamical instabilities. The new term $\Pi_{ij}^{(2)}$ given by equation (25) of artificial viscosity comes from the diagonal of the stress tensor so its contribution to shear viscosity is probably lower than that of $\Pi_{ij}^{(1)}$. In any case, the artificial viscosity formulation given in this work is so close to the standard formulation that it could benefit from future advances in the much better studied three-dimensional SPH. Finally, the simple test about the implosion of a rotating cylinder indicates that axisymmetric SPH is able to handle rotating structures but more work needs to be done to incorporate angular momentum transport into the numerical scheme.

ACKNOWLEDGMENTS

The authors want to thank the many corrections and suggestions made by the referee. In particular, the referee suggested the inclusion of the Noh test and the bubble collision scenario described in Sections 4.4 and 4.5 and inspired the discussion about rotation given in Section 3.3.1. This work has been funded by Spanish DGICYT grants AYA2005-08013-C03-01 and was also supported by DURSI of the Generalitat de Catalunya.

REFERENCES

Blondin J. M., Lundqvist P., Chevalier R. A., 1996, ApJ, 472, 257
Brookshaw L., 1985, Proc. Astron. Soc. Aust., 6, 207
Brookshaw L., 2003, ANZIAM J, 44, C114
Cabezón R., García-Senz D., Relaño A., 2008, J. Comput. Phys., 227, 8523
Gingold R. A., Monaghan J. J., 1977, MNRAS, 181, 375
Herant M., Benz W., 1992, ApJ, 387, 294
Hernquist L., Katz N., 1989, ApJS, 70, 419
Jubelgas M., Springel K., Dolag K., 2004, MNRAS, 351, 423
Lucy L. B., 1977, AJ, 82, 1013
Monaghan J. J., 1989, J. Comput. Phys., 82, 1
Monaghan J. J., 1992, Annu. Rev. Astron. Astrophys., 30, 543
Monaghan J. J., 2005, Rep. Prog. Phys., 68, 1703
Monaghan J. J., Gingold R. A., 1983, J. Comput. Phys., 52, 374
Noh W. F., 1987, J. Comput. Phys., 72, 78
Omang M., Borve S., Trulsen J., 2006, J. Comput. Phys., 213, 391
Omang M., Borve S., Trulsen J., 2007, Shock Waves, 16, 467

Owen J. M., Villumsen J. V., Saphiro P. R., Martel H., 1998, ApJS, 116, 155
Petscheck A. G., Libersky L. D., 1993, J. Comput. Phys., 109, 76
Velarde P., García-Senz D., Bravo E., Ogando P., Relaño A., García C., Oliva E., 2006, Phys. Plasmas, 13, 092901

APPENDIX A: CORRECTION FACTORS CLOSE TO Z-AXIS

First, we derive the factor f_1 affecting the two-dimensional density η. Close to the Z-axis symmetry enforces the three-dimensional density ρ to have a maximum or a minimum. Thus, we can safely assume $\rho = \rho_0$ in the axis vicinity. If we make the one-dimensional SPH estimation of the averaged density along the r-axis,

$$\langle \eta(r) \rangle = \int_{-\infty}^{\infty} \eta(r') W^{1D} \left(\frac{|r - r'|}{h} \right) \mathrm{d}r', \tag{A1}$$

where $W^{1\mathrm{D}}$ is the cubic-spline kernel in one dimension:

$$W^{1\mathrm{D}}(u_r) = \frac{2}{3h} \begin{cases} 1 - \frac{3}{2}u_r^2 + \frac{3}{4}u_r^3 & 0 \le u_r \le 1 \\ \frac{1}{4}(2 - u_r)^3 & 1 < u_r \le 2 \\ 0 & u_r > 2 \end{cases} \tag{A2}$$

being $u_r = |(r - r')|/h$. If we take $\eta(r') = 2\pi|r'|\,\rho_0$, which is only valid for $r' \to 0$,

$$\langle \eta(r) \rangle = 2\pi\rho_0 \int_{-\infty}^{\infty} |r'| W^{1\mathrm{D}} \left(\frac{|r - r'|}{h} \right) \mathrm{d}r'. \tag{A3}$$

Using the cubic-spline the right-hand side of equation (A3) can be integrated to give:

$$\langle \eta(r) \rangle = \frac{\widehat{\eta}}{f_1(\zeta)}, \tag{A4}$$

where $\zeta = r/h$, and $\widehat{\eta} = 2\pi r\rho$ is the corrected density (hereafter we put a hat over any corrected quantity). The correction factor $f_1(\zeta)$ is given by equation (5). The density in brackets is what SPH computes using summatories instead of integrals. Thus, adding the z-coordinate and using $W^{2\mathrm{D}}$ the corrected density can be evaluated using

$$\widehat{\eta}(r) = \langle \eta \rangle f_1(\zeta) = \left(\sum_{j=1}^{N} m_j W^{2\mathrm{D}}(|\boldsymbol{r_i} - \boldsymbol{r_j}|, h_i) \right) \times f_1^i. \tag{A5}$$

A similar procedure can be used to get the adequate expressions for ηv_r and ηv_z, needed to compute the temporal evolution of density, equation (15). Symmetry enforces the radial velocity to vanish at the symmetry axis, thus close to that axis $v_r = Cr$ and

$$\langle \eta v_r \rangle = \rho(z) 2\pi K^{1\mathrm{D}} C \int_{-\infty}^{\infty} |r'| r' W^{1\mathrm{D}}(u_r)\, \mathrm{d}r'. \tag{A6}$$

Again the integral on the right-hand side admits an analytical solution for the cubic-spline kernel. After a little algebra, the following expression is obtained:

$$\langle \eta v_r \rangle = \frac{\widehat{\eta v_r}}{f_2(\zeta)}, \tag{A7}$$

where $f_2(\zeta)$ is given by equation (16). The expression inside the brackets is what the numerical code calculates using summatories instead of integrals. Thus, the corrected $\widehat{\eta v_r}$, value of that magnitude is

$$(\widehat{\eta v_r})_i = \left(\sum_{j=1}^{N} m_j v_{r_j} W(|\boldsymbol{s_i} - \boldsymbol{s_j}|, h_i) \right) \times f_2^i. \tag{A8}$$

Similarly, the correction to be applied to ηv_z is

$$\langle \eta v_z \rangle = \frac{\widehat{\eta v_z}}{f_1(\zeta)}, \tag{A9}$$

and its corresponding discrete expression is

$$(\widehat{\eta v_z})_i = \left[\sum_{j=1}^{N} m_j v_{z_j} W(|\boldsymbol{s_i} - \boldsymbol{s_j}|, h_i) \right] \times f_1^i. \tag{A10}$$

A plot of the factors $f_1(\zeta)$ and $f_2(\zeta)$ and their radial derivatives are given in Fig. 1. The factor $f_1(\zeta)$ is exactly one for $r = 2h$ and goes to zero when $r/h \to 0$, as expected. However, it can be seen that factor $f_2(\eta)$ is close but not exactly one at $r = 2h$ and its slope is not totally flat. This is because the integral expression in equation (A6) is quadratic in the radial coordinate r thus the interpolation does not give the exact value of $\langle \eta v_r \rangle$.

This paper has been typeset from a TEX/LATEX file prepared by the author.